Proceedings of the Estonian Academy of Sciences,
2023, **72**, 2, 115–127
https://doi.org/10.3176/proc.2023.2.03
Available online at www.eap.ee/proceedings

MATERIAL
SCIENCE

Comparison of multifractal parameters of surface defects and non-defects

Merike Martsepp[a*], Tõnu Laas[a], Siim Tõkke[a], Jaanis Priimets[a,b] and Valdek Mikli[c]

[a] Tallinn University, School of Natural Sciences and Health, Uus-Sadama 5, 10120 Tallinn, Estonia
[b] Tallinn University of Technology, Estonian Maritime Academy, Kopli 101, 11712 Tallinn, Estonia
[c] Tallinn University of Technology, Laboratory of Optoelectronic Materials Physics, Ehitajate tee 5, 19086 Tallinn, Estonia

Received 29 September 2022, accepted 1 February 2023, available online 16 March 2023

Abstract. In this study, three different materials (pure tungsten and two tungsten alloys with Fe and Ni dopants), which have been irradiated with a high-temperature deuterium plasma of 20, 25 and 100 plasma shots, are considered. The multifractal characteristics obtained from SEM images are then compared for the same specimens by analysing the distribution of defects and non-defects (non-damaged areas). A valid tendency was found that the brighter the original input image, the more accurate the results obtained when examining a non-damaged surface using multifractal characteristics.

Keywords: defects, multifractal analysis, non-defects, plasma, SEM, tungsten, tungsten alloys.

1. INTRODUCTION

Tungsten, which is known to have a high melting point, and its alloys, have great potential to be used in fusion reactor internal chamber designs [1–3] because of their excellent mechanical properties. Since pure tungsten is brittle at high temperatures, various materials containing tungsten have been tested, such as double-forged tungsten, nanowire-enhanced tungsten fibers, etc. [4–8]. Tungsten is also alloyed with yttrium oxide, tantalum, potassium, titanium carbide, rhenium, etc., for the same purpose [9–18]. In this study, we compare the damage made by plasma fluxes on pure tungsten [19] with its two dual-phased alloys containing 5% and 3% nickel-iron dopants [20].

Fractal and multifractal analysis, which has gained popularity in the last few decades, can be practiced in several different fields, e.g. in the study of geological processes [21], heart rhythms [22], city planning [23], and in the exploration of complex payment networks [24]. However, it has mostly been applied to research and to describe various surface structures [25–35], and is, therefore, suitable for studying specific surface defect structures (such as cracks and a mesh of cracks, blisters, traces of erosion, wavy formations, etc.) from plasma-irradiated surfaces. By using the concept of multifractals, in addition to the usual descriptive methods [20], quantitative values and graphs characterizing the surface damage structures as a whole can be studied [22, 36–38]. The box-counting technique can be applied to surfaces of a defected material as well as to the same surfaces of non-defects (without a defected area). It is obvious that the sum of probabilities of the area being defected or not defected is one.

Considering the probabilities that the area (part of the whole sample) contains damaged points, we can calculate the monofractal dimension, which characterizes the distribution of the damage. Multifractal formalism and multifractal dimension are used, e.g. in assessing the level of surface damage – whether big or small defects dominate. However, the use of the Legendre transform usually applied to the calculation of a new pair of multifractal parameters, is restricted by additional requirements for the multifractal dimension.

* Corresponding author, martsepp@tlu.ee

Moreover, if we calculate mono- or multifractal characteristics of the defected or not defected areas of the same surface, we find that the mathematical results obtained for defects do not correspond to those of non-defects and vice versa. If we apply multifractal (MF) formalism to find a distribution of the non-damaged areas (non-defects), it appears that the Legendre transforma can be used and, therefore, a full multifractal spectrum can be analysed.

In this study, we take a closer look at the MF characteristics obtained from surface defects versus non-defects and recommend the appropriate usage of each of them in research.

2. EXPERIMENTAL SETUP AND METHODS

This study compares three different materials:

1) Pure tungsten (>99.97% W), sample size approx. 12 × 15 × 2 mm^3. The distance between the sample and the anode was 6 cm. The specimens were irradiated with 20 and 100 plasma pulses.
2) Dual-phase tungsten alloy (HPM1850) with 97% W, 1% Fe and 2% Ni, approx. 15 × 15 × 5 mm^3. The distance between the sample and the anode was 6.5 cm. The specimens were irradiated with 25 and 100 plasma pulses.
3) Dual-phase tungsten alloy (HPM1800) with 95% W, 1.67% Fe and 3.33% Ni, approx. 15 × 15 × 5 mm^3. The distance between the sample and the anode was 6.5 cm. The specimens were irradiated with 25 and 100 plasma pulses.

Prior to irradiation with deuterium plasma in a PF-12 plasma focus device with a heat flux factor of 160 MW · s^{½} · m^{-2}, all samples were polished mirror-smooth so that the average micro-roughness was less than 0.3 μm. Irradiation of the tungsten or tungsten alloys by the plasma with the abovementioned heat flux factor leads to partial melting of the surface layer. Therefore, repeated plasma pulses and heating-cooling cycles cause various damage to the surface of the test pieces, such as macrocracks, microcracks, a mesh of cracks, erosion residues, blisters, and bumps. The experimental conditions can be found in more detail in previous studies [19,20]. The deformed surfaces of the test specimens were then imaged with a Zeiss EVO MA-15 scanning electron microscope (SEM) with an acceleration voltage of 20 kV and a working distance of 9 cm. To get the SEM images for analysis, 500x magnification was used, which gave images of 768 × 1024 pixels.

The MF analysis program written in Mathematica 11 was then applied to the SEM images previously cut into 768 × 768 pixels. Before the application of MF analysis, we applied the binarization process to the SEM images. If the greyness value of the pixel was greater than 0.5, the value was taken as one and vice versa.

In brief, the principle of the box-counting method is to cover the surface of the test piece with sets of squares. Each such set of squares has a characteristic edge size ε, and the number of squares required to cover the test piece is $N(\varepsilon)$. In this study, the side lengths of the squares were $\varepsilon = 2, 4, 8, 16, 32, 64$ (i.e. $\varepsilon = 2^k$, $k = 1, 2, 3, 4, 5, 6$) pixels. We get the distribution of the probability of the defect in the i-th box $P_i(\varepsilon)$ by calculating the pixels defined as the damages remaining in one box φ_i as

$$P_i(\varepsilon) = \frac{\varphi_i(\varepsilon)}{\sum_{i=1}^{n}(\varphi_i(\varepsilon))}. \quad (1)$$

Next, the partition function $\chi_P(\varepsilon)$ is calculated considering the moment order q:

$$\chi_P(\varepsilon) = \sum_{i=1}^{n}[P_i(\varepsilon)]^q \propto \varepsilon^{\tau(q)}, \text{ when } \varepsilon \to 0, \quad (2)$$

where $\tau(q)$ is the mass exponent. If the MF property of damage distribution on the surface exists, the power-law relationship between the partition function χ_P and the scale ε is valid:

$$\log \chi_P(\varepsilon) \propto \tau(q) \log \varepsilon, \quad (3)$$

where $\tau(q)$ can be calculated as a slope of a linear function. The generalized fractal dimension $D(q)$ is given by

$$D(q) = \frac{\tau(q)}{q-1} = \frac{1}{q-1} \cdot \lim_{\varepsilon \to 0}\left[\frac{\log \chi_P(\varepsilon)}{\log \varepsilon}\right], \quad q \neq 1 \quad (4)$$

$$D(q) \approx \lim_{\varepsilon \to 0}\left[\sum_{i=1}^{n}\frac{P_i(\varepsilon)\log P_i(\varepsilon)}{\log \varepsilon}\right], \quad q = 1. \quad (5)$$

In the monofractal case, $D(q)$ is a constant for all q values. In the ideal multifractal case, $D(q)$ is a monotonous function of q. The dependence of the generalized dimension D on q allows us to estimate the role played by rare events (or rare defects, or rare structures) and frequent events. The values of negative q enhance the role of rare events and the values of positive q the role played by frequent events [19]. If $D(q)$ decreases when q increases, so that $D(0) > D(1) > D(2)$, then we can say that rare but large defects (structures) dominate frequent but small defects (structures).

In this paper, we compare the distribution of structures of defects with the distribution of structures of non-defects.

Another set of parameters characterizing the multifractality of the distribution of defects (or non-defects) is $f(\alpha(q))$ and $\alpha(q)$ given by the Legendre transform:

$$f(\alpha(q)) = q \cdot \alpha(q) - \tau(q), \quad (6)$$

where the singularity exponent $\alpha(q)$ is defined by slope of the mass exponent $\tau(q)$:

$$\alpha(q) = \frac{d\tau(q)}{dq}. \quad (7)$$

Although this transform can be done if $D(q)$ is a non-linear monotonously decreasing function of q, in applications, however, this transform can also be done if $D(q)$ is a monotonously increasing function of q, or for the region, where the monotonous behavior of $D(q)$ is valid.

The function $f(\alpha)$ is the multifractal spectrum of the set of boxes, where α (the Legendre transform) is derived from τ by some exponent of q that varies over the fractal. Δf represents the ratio of the number of boxes with the highest probability to the number of boxes with the lowest probability. When the fragments with a higher probability value dominate (i.e. there are more of them), then $\Delta f > 0$. Conversely, when the fragments that are mainly characterized by low probability dominate, $\Delta f < 0$.

In the case of a monofractal, the pattern changes evenly – this means that the probability distribution is slightly distorted when the sets of squares are exchanged. In the case of a multifractal, however, the pattern changes unevenly, and different mathematical aspects emerge from the graphs for both $D(q)$ vs q and $f(\alpha)$ vs α. The multifractal spectrum $f(\alpha)$ vs α is a graph with a small hump for monofractals, but the more multifractal the surface the more it contributes to the breadth of that bump, and for that reason, we have calculated Δf, the width of the bump (see also Table 1). With respect to monofractals and non-fractals, the graph $D(q)$ vs q has a small variance, while for multifractals, $D(q)$ usually decreases with a decrease in q, which often occurs sigmoidally before the point $q = 0$. Details of the application of the MF theory and the box-counting method can be found in the articles of previous studies [36,37].

In addition to the preceding studies, this time the MF parameters of the damaged (non-defects marked in black) and undamaged parts (defects marked in black) of the surfaces of the same specimens have been compared. Multifractal analysis was applied to white pixels in a binarized SEM image (see Fig. 1).

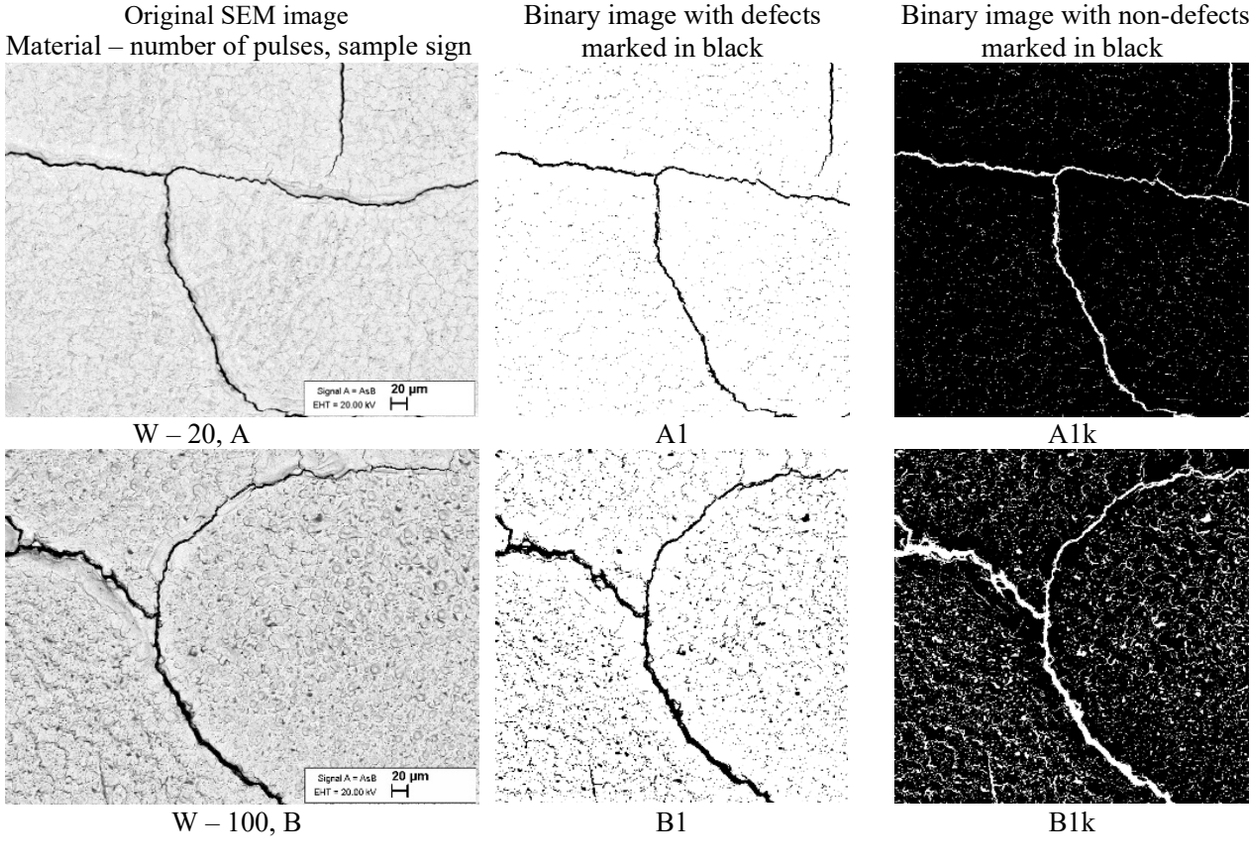

Fig. 1. Original SEM image (with magnification 500x) of each test piece examined – left column, the binarized images corresponding to the images on which the non-defect analyses were performed – middle column, and the corresponding defect analysis input images – right column. (*Continued on the next page*)

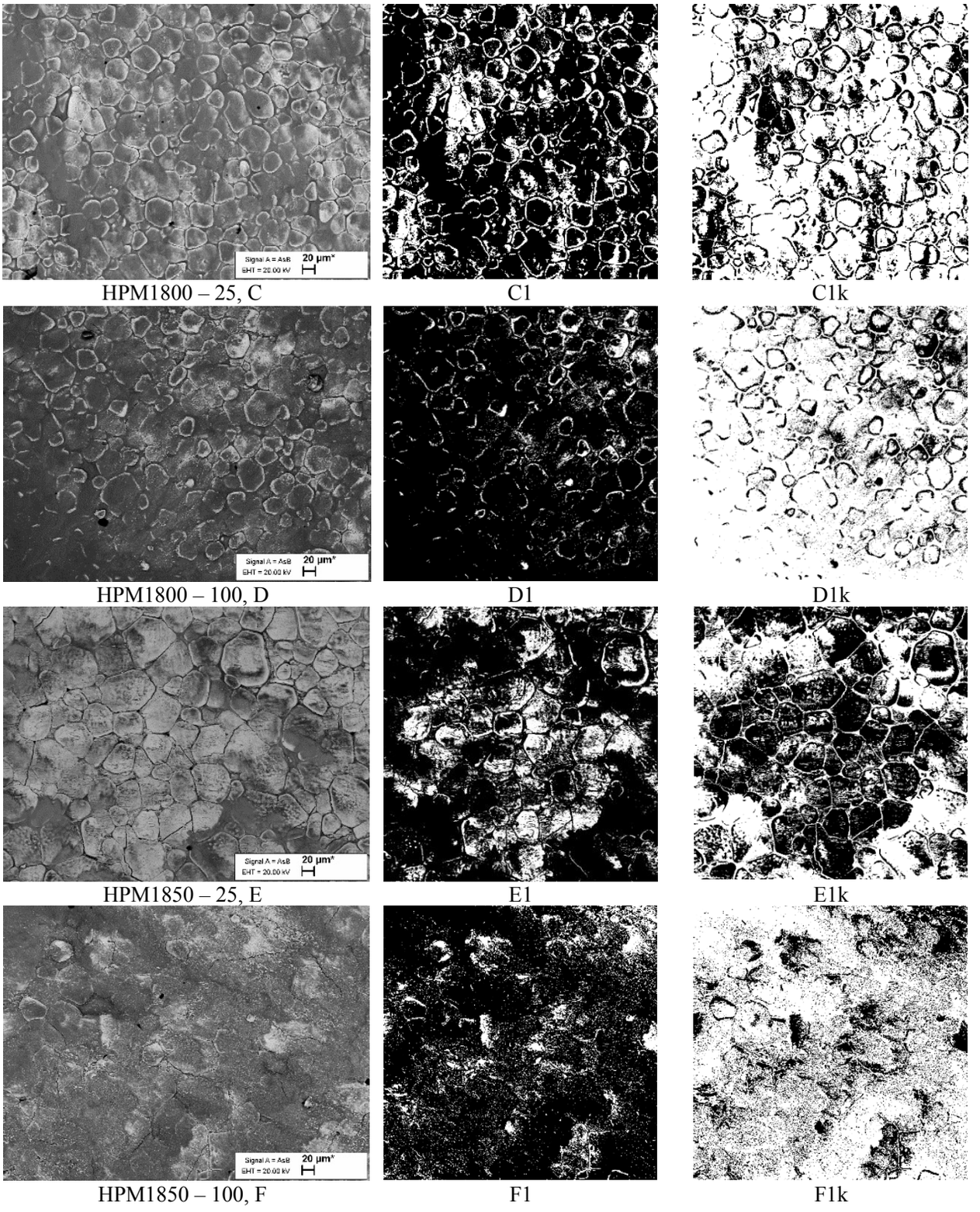

Fig. 1. *Continued.*

3. RESULTS AND DISCUSSION

3.1. Comparison of SEM pictures

In Fig.1, a selection of raw data and binarized images are shown, from which can be seen that the SEM images of pure tungsten are brighter than tungsten alloys with 3% or 5% impurity, regardless of the number of plasma pulses. It is also worth mentioning how, in addition to the above, even a small percentage of impurity makes the surface structure different, so that it is no longer so brittle as to crack easily. While the surface of W is dominated by large cracks and wavy formations, Ni and Fe have melted from between the grains of alloys HPM1800 and HPM1850, revealing a peculiar granular structure. In a very rough approximation, we can say that in the case of tungsten the main or dominating defects are the cracks, and in the case of tungsten alloys the dominating defects are the melting traces of the second phase (FeNi).

'k' at the end of picture and graph names denotes the word '*kahjustus*' – 'damage' in Estonian, since 'D' already has a meaning in the box-counting method of multifractal analysis.

3.2. Comparison of MF analysis of surface defects and non-defects

In Figs 2 and 3, for each graph, A, B, C, D, and E denote the graphs calculated from the non-defects in the surface area of the specimens, and Ak, Bk, Ck, Dk, and Ek denote the graphs calculated from the defects in the surface of the specimens, respectively. A, B, C, D, E are images of test pieces prepared under the same conditions, i.e. ideally their graphs should overlap and have the same values at all points.

The general fractal dimension plots describing the non-defects of the surfaces in the range $-2 < q < 5$ in Fig. 2a practically overlap, but the same does not apply to the corresponding plots describing the defects, where the plots $-5 < q < 2$ are particularly scattered with respect to each other. A similar trend can be seen later in Fig. 3a for the fractal spectra of the same test pieces. The most important numerical values for the fractal characteristics of the graphs in Figs 2a and 3a are displayed in Table 1, which accurately shows the average values of the MF analysis calculated from defects and non-defects, with corresponding standard deviations (SD). For material W20, it can be said that the SD in the MF analysis of the defects is larger than for the areas of non-defects.

The interpretation of $D(q)$ for non-defects allows us to suggest that, as $D(-5) > D(5)$, then for a non-defects area, big but infrequently connected non-damaged areas dominate over frequent but fractured and not-connected non-damaged areas (Table 1; Fig. 2a). This is confirmed by the value of $\Delta f = -1.635 > 0$, as well. Small SD values allow us to suggest that one separate SEM image of the specimen can be used for a conclusion about the distribution of non-defects. When we consider the damaged areas, then $D(q)$ for W20Bk changes less than for other graphs. The $D(q)$ for W20Ak, W20Bk, W20Ck is non-monotonous in the current range of q, and thus we cannot apply the Legendre transform to this. Nevertheless, the interpretation of the average values of D(q) for defects on W20 allows us to suggest that frequent small defects dominate over the areas of rare big defects. This conclusion is in accordance with the conclusion about the distribution of non-defects. However, as $\Delta f = -0.724 > 0$, we could conclude that fragments with lower probabilities dominate, which contradicts the conclusion from the analysis of D(q). This is mainly because the Legendre transform was valid only for part of the values of q.

In Fig. 2b, essentially the same trend continues for the graphs of both non-defects and defect-describing surfaces of W100. In Fig. 2b, the non-defect graphs are slightly more scattered than in Fig. 2a, which is also understandable, since in the first case the test pieces received only 20 shots and in the second case 100 plasma shots, so in the second case the surfaces should be more damaged and thus more multifractal. In addition, Fig. 1 reveals from the SEM images A and B that for W100 the cracks are deeper and the melting marks are more noticeable than for W20. We can make the same conclusions of distribution for non-defects as for W20 (see also Table 2). However, we cannot apply the same simple interpretation to graphs describing defects because they are not monotonic. From the difference of the values of average $D(-5)$ and $D(5)$ (and considering the SD) we can say that both, small and big defects are with the same probabilities. But the Legendre transform cannot be used for all ranges of q and cannot be used for the analysis, and thus Δf can be used for a small range of the multifractal dimension values (see also Table 3).

In Fig. 2c (where instead of five specimens we are considering two specimens A and B and the corresponding defect analysis Ak and Bk for both 25 and 100 shots; the same logic applies to Fig. 2d), it is observable that both A and B as well as Ak and Bk give very similar graphs; the same emerges in both 100 shot and 25 plasma shot cases (see Tables 2 and 3 for values of $D(-5)$–$D(5)$, Δf and their standard deviations). Another notable difference from the graphs of pure tungsten is that the analysis of the non-defect surface gives lower $D(q)$ values than the analysis of the defective surface. The latter observation is better understood by looking at the examples of the corresponding images in Fig. 1, namely that the SEM images of the alloy HPM1800 are already darker than those of pure tungsten, and, consequently, the defects are markedly darker and the non-defects lighter.

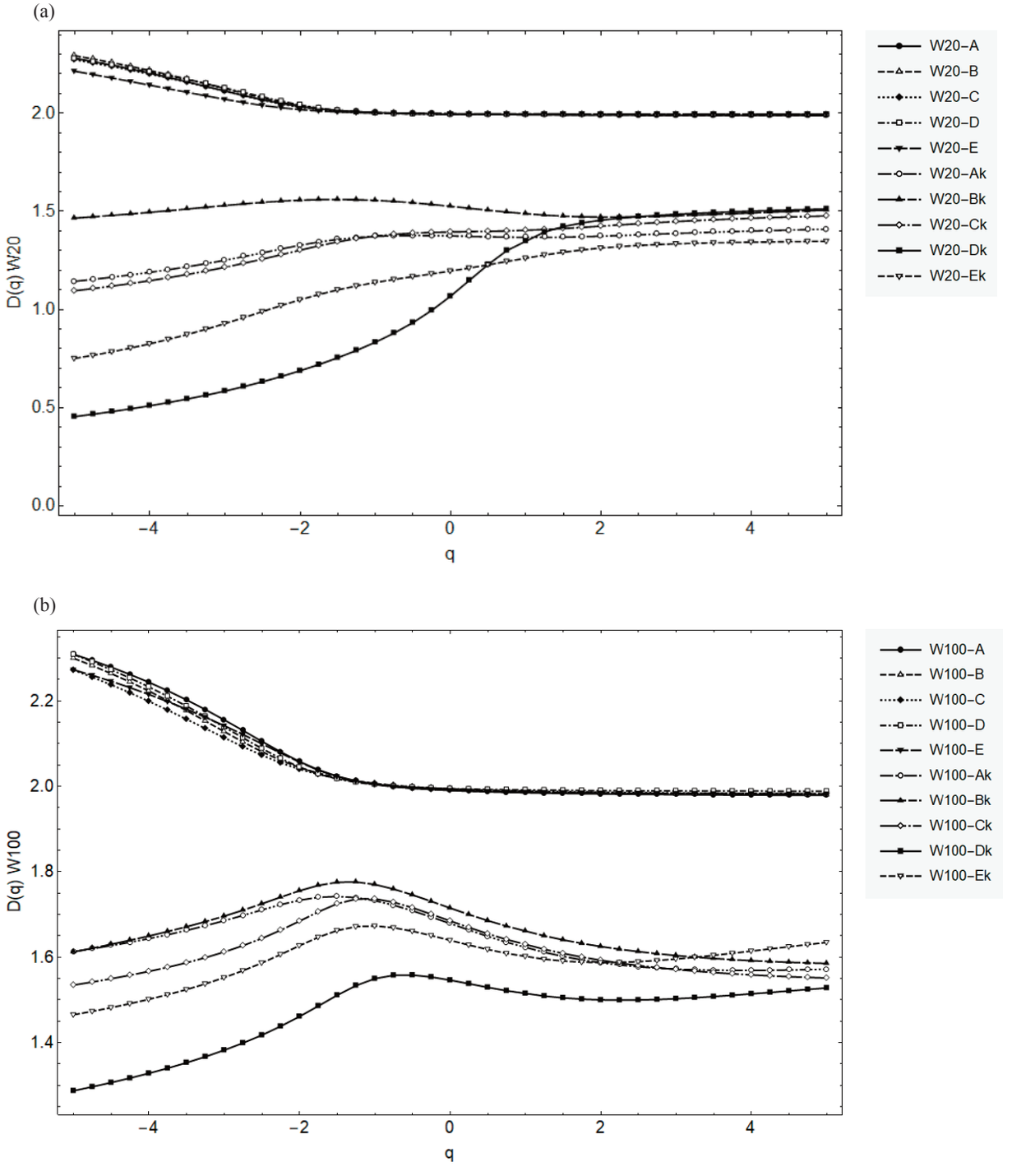

Fig. 2. Generalized multifractal dimension $D(q)$ vs q plots divided by different materials: (a) – W20, (b) – W100, (c) – HPM1800, (d) – HPM1850 (HPM is omitted from the legend for shortage of space). (*Continued on the next page*)

(c)

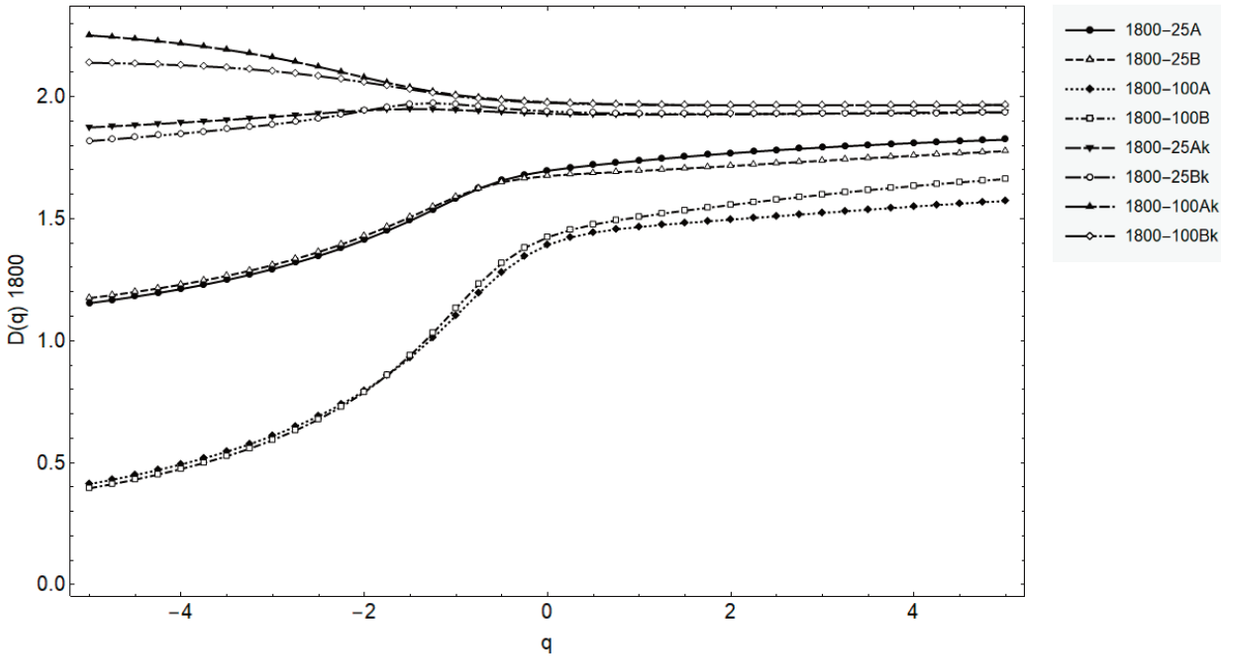

(d)

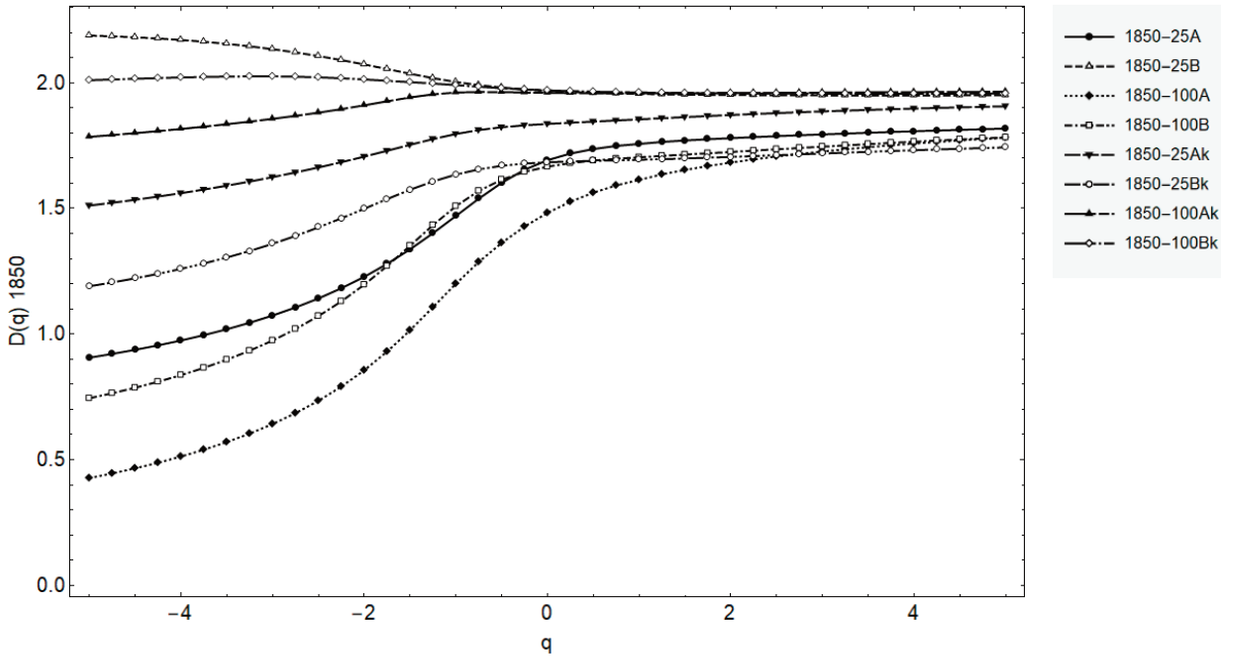

Fig. 2. *Continued.*

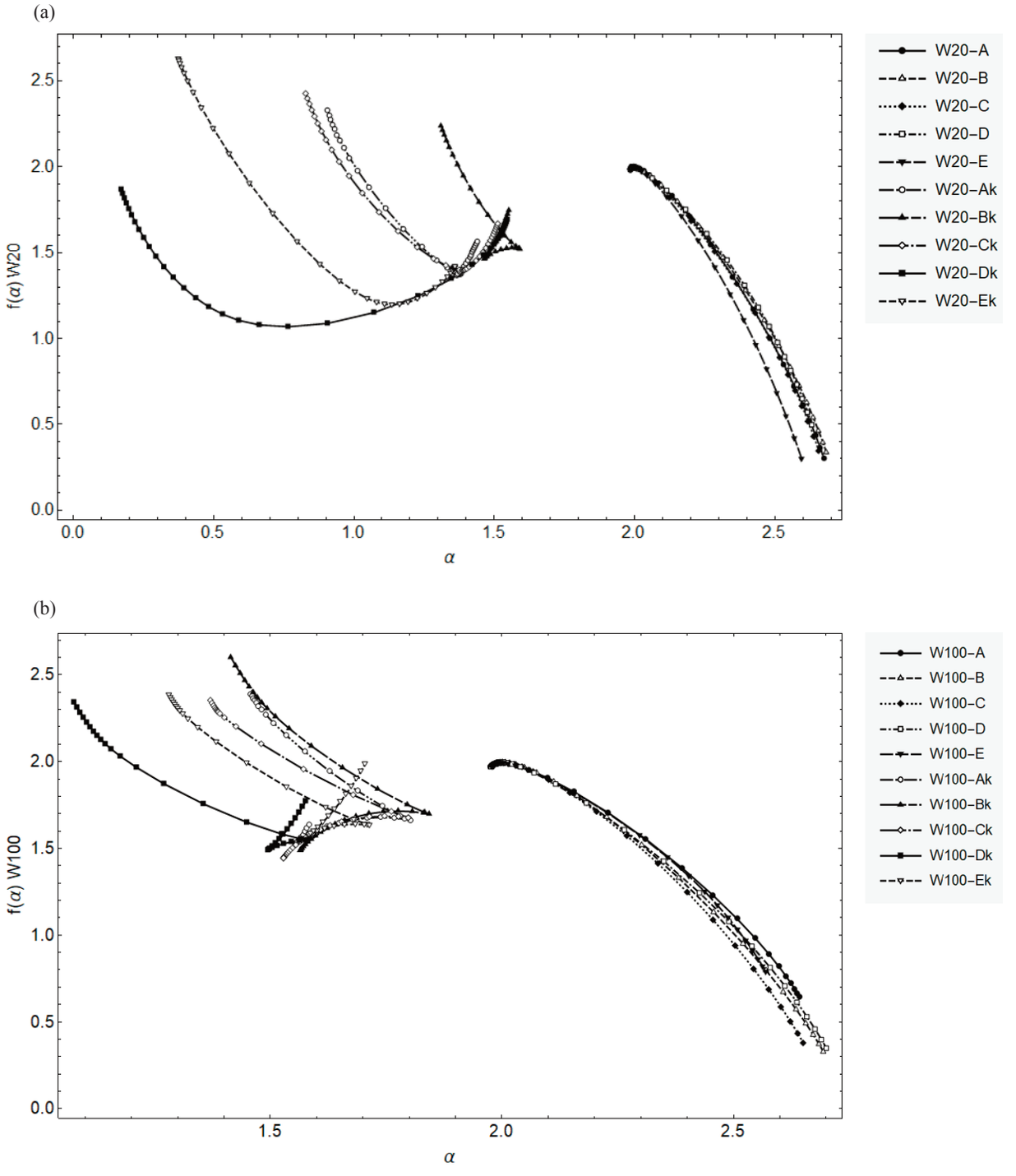

Fig. 3. Multifractal spectrum $f(\alpha)$ vs $\alpha(q)$ plots divided by different materials: (a) – W20, (b) – W100, (c) – HPM1800, (d) – HPM1850.
(*Continued on the next page*)

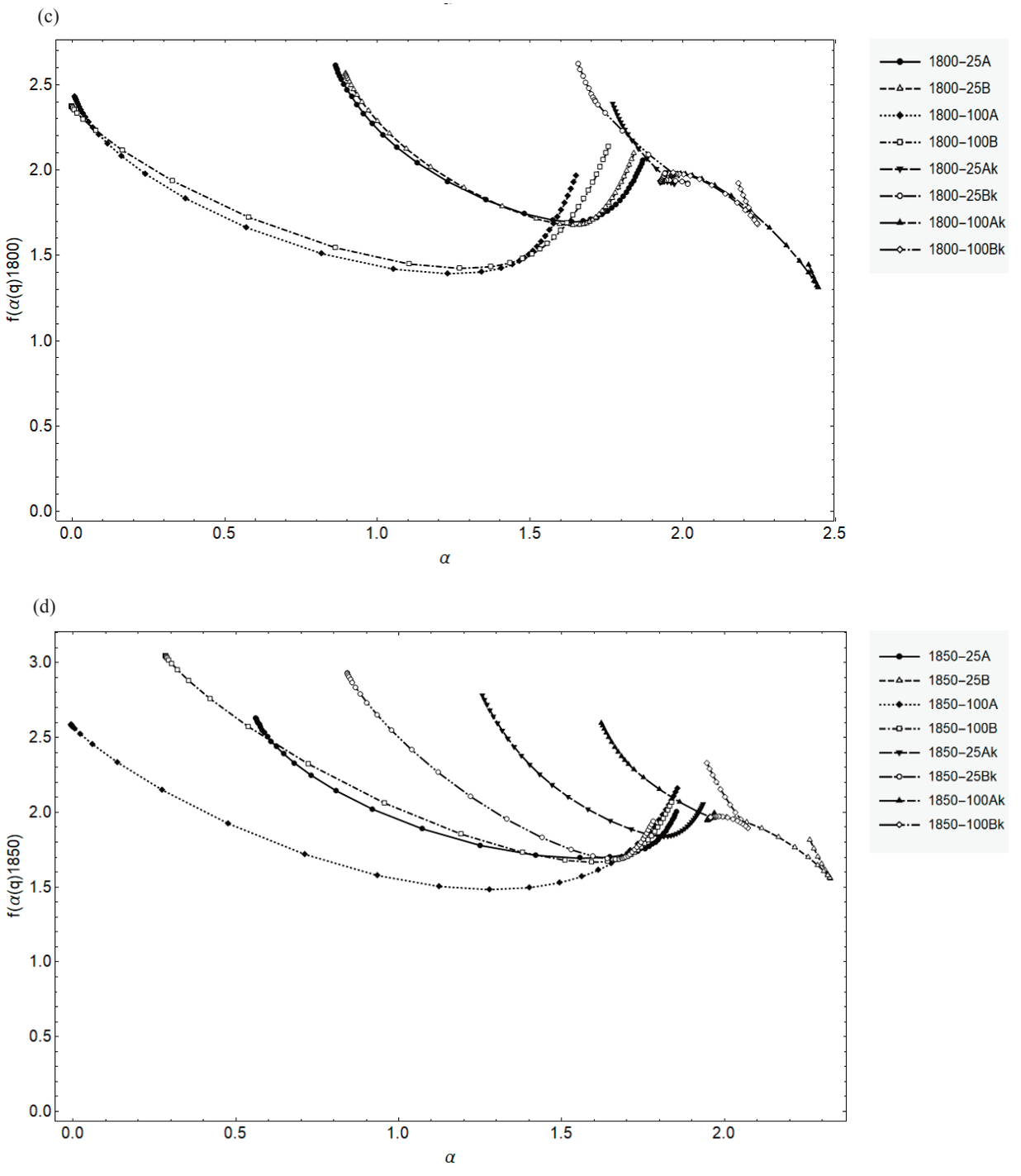

Fig. 3. *Continued.*

Table 1. Selected numerical values of the fractal characteristics, their averages, and standard deviations of the graphs in Fig. 2a and Fig. 3a for W20

MF parameter	Average	Average 'k'
D (–5)	2.267 ± 0.031	0.982 ± 0.389
D (0)	1.996 ± 0.021	1.312 ± 0.180
D (1)	1.994 ± 0.002	1.374 ± 0.083
D (2)	1.993 ± 0.002	1.408 ± 0.064
D (5)	1.992 ± 0.003	1.450 ± 0.071
α (max)	2.650 ± 0.035	1.491 ± 0.092
α (0)	1.999 ± 0.002	1.247 ± 0.309
α (1)	1.994 ± 0.002	1.374 ± 0.083
α (2)	1.992 ± 0.003	1.430 ± 0.063
α (min)	1.991 ± 0.003	0.719 ± 0.452
Δα = α(max) – α(min)	0.659 ± 0.038	0.772 ± 0.423
f(α(max))	0.354 ± 0.081	1.572 ± 0.118
f(α(0))	1.996 ± 0.001	1.312 ± 0.180
f(α(1))	1.994 ± 0.002	1.374 ± 0.083
f(α(2))	1.992 ± 0.003	1.453 ± 0.067
f(α(min))	1.98 ± 0.006	2.296 ± 0.280
Δf = f(α(max)) – f(α(min))	–1.635 ± 0.079	–0.724 ± 0.368

Table 2. The averages of the extreme points of the generalized multifractal dimension $D(q)$ of all test objects, their differences, and the standard deviation of the parameters

MF parameter	D(–5)	D(5)	D(–5)–D(5)	D(–5)	D(5)	D(–5)–D(5)
specimen	non-damage	non-damage	non-damage	damage	damage	damage
W20	2.267 ± 0.031	1.992 ± 0.003	0.275 ± 0.033	0.982 ± 0.389	1.450 ± 0.071	–0.469 ± 0.386
W100	2.293 ± 0.019	1.983 ± 0.003	0.310 ± 0.019	1.503 ± 0.136	1.574 ± 0.04	–0.072 ± 0.126
HPM 1800 25	1.164 ± 0.015	1.800 ± 0.033	–0.636 ± 0.048	1.846 ± 0.040	1.936 ± 0.002	–0.090 ± 0.034
HPM 1800 100	0.404 ± 0.013	1.618 ± 0.063	–1.214 ± 0.076	2.195 ± 0.079	1.966 ± 0.0002	0.229 ± 0.080
HPM 1850 25	1.547 ± 0.906	1.884 ± 0.094	–0.337 ± 0.813	1.351 ± 0.227	1.825 ± 0.115	–0.474 ± 0.112
HPM 1850 100	0.586 ± 0.225	1.782 ± 0.001	–1.196 ± 0.224	1.898 ± 0.160	1.961 ± 0.005	–0.063 ± 0.165

However, the similarities in the graphs noted above (test pieces irradiated with the same material and under the same conditions give resembling plots in the MF analysis) do not apply in Fig. 2d to the alloy HPM1850. Both A and B as well as Ak and Bk give different results for both 100 and 25 plasma shots. Nevertheless, in Fig. 1, we can see that, similarly to the HPM1800, the original images are quite dark (due to melting of the FeNi phase and copper marks), thus causing a pronounced darkness of defects and a brightness of non-defects. Looking at the images in Fig. 1 alone, it cannot be said that C and D are much more special than E or F, but the MF analysis shows that there is a significant difference between the two tungsten alloys. The HPM1850 graphs are more diffuse in the drawing (see also Tables 2, 3), making them more multifractal, so one could expect them to be more damaged. (A separate question is whether this is true or is a feature of the MF analysis because binarization turns all areas with more than 50% darkness in the image black and less than 50%, white.) Although each graph is considered in Fig. 2d unique, their trajectories converge in the initial range $0.4 < D < 2.2$ to the range $1.7 < D < 2$. A comparable tendency occurs in Fig. 2c and somewhat in the case of Fig. 2a.

In Fig. 3, we see a similar trend for a and b in the multifractal spectra as in graphs a and b in Fig. 2 for the general fractal dimension of pure tungsten. In both graphs (in Figs 2a,b), A, B, C, D, E are in the range of

Table 3. The averages of the extremum points of the multifractal spectrum $f(\alpha)$ of all test objects and their differences, together with their standard deviation. *$\Delta f = f(\alpha(Max)) - f(\alpha(Min))$

MF parameter	f(α(max))	f(α(min))	Δf*	f(α(max))	f(α(min))	Δf*
specimen	non-damage	non-damage	non-damage	damage	damage	damage
W20	0.354 ± 0.081	1.989 ± 0.006	–1.635 ± 0.079	1.571 ± 0.118	2.296 ± 0.281	–0.724 ± 0.368
W100	0.496 ± 0.207	1.973 ± 0.008	–1.477 ± 0.207	1.643 ± 0.058	2.413 ± 0.106	–0.770 ± 0.086
HPM 1800 25	2.076 ± 0.029	2.588 ± 0.032	–0.512 ± 0.062	1.918 ± 0.000	2.505 ± 0.167	–0.588 ± 0.167
HPM 1800 100	2.052 ± 0.121	2.400 ± 0.042	–0.3499 ± 0.162	1.495 ± 0.262	1.963 ± 0.001	–0.468 ± 0.261
HPM 1850 25	1.778 ± 0.315	2.287 ± 0.484	–0.510 ± 0.169	1.996 ± 0.081	2.853 ± 0.104	–0.858 ± 0.186
HPM 1850 100	2.112 ± 0.066	2.810 ± 0.332	–0.699 ± 0.399	1.943 ± 0.071	2.461 ± 0.189	–0.518 ± 0.118

about $2 < \alpha < 2.7$; in the case of W20 (in Fig. 3a), Ak, Bk, Ck, Dk, Ek are in the range of about $0.2 < \alpha < 1.6$; and in the case of W100 (in Fig. 3b), in the range of about $1.35 < \alpha < 1.85$, which means that for more plasma shots, the surface damage analyses become more similar. Although the decrease in the range of the spectrum suggests less damage, the shapes of the graphs must also be considered. The graphs with 'k' are concave for a and zigzag for b, while the graphs for non-defect analysis are convex in both cases in the same figure. The shape of the zigzag graph suggests that this result cannot be well measured objectively by the MF analysis. Makowiec [22] acknowledges that such peculiar shapes arise when non-monotonic functions are transformed into Legendre, which happens when small numbers are considered.

Figure 3c is similar to the results of the same test piece in Fig. 2c, where both A and B as well as Ak and Bk are very close to each other's graph. However, when examining fractal spectra, there is already a slight difference in the analysis of 'k' or surface defects between Ak and Bk, although they are still similar to each other for both 25 and 100 plasma shots as in the other pairs in Fig. 3c.

Similarly to Fig. 2d, all graphs in Fig. 3d appear to be different without any strong correlations between them. They are mostly concave, although a few pieces are slightly convex with 'long arms' due to non-monotonic dependence of D on q.

Overall, for the test specimens, in terms of the fractal spectrum in all parts (a, b, c, d) of Fig. 3, the defected area graphs marked 'k' have an unusual shape, whether concave or zigzag. At the same time, the fractal spectrums of non-defected areas of pure tungsten (a and b) give nice curved and interpretable graphs; however, the analogous tendency does not apply to tungsten alloys HPM1800 and HPM1850.

Generally, for both defects and non-defects, the graphs of $D(q)$ are monotonic, and the Legendre transform can be performed. There also appears to be a tendency for the decreasing non-defect $D(q)$ to be matched by the increasing defect $D(q)$. However, in some cases (such as W100), the Legendre transform cannot be strictly applied to defects, and the interpretation of the $D(q)$ graph is also difficult. In such cases, we would recommend using the so-called non-defect analysis.

4. CONCLUSIONS

Deuterium plasma was used to irradiate test specimens of pure tungsten (with 20 and 100 pulses) and two tungsten alloys, one containing 1% Fe and 2% Ni, the other 1.67% Fe and 3.33% Ni (with 25 and 100 pulses). The multifractal graphs of defects and non-defects were then compared from their SEM images using the MF analysis box-counting method. The study revealed:

1) There is a tendency that the brighter the original SEM image, the better the results of the non-damage examination using the box-counting method. For brighter SEM images, the MF analysis of the undamaged surface results in characteristics that are generally more similar (with less error) than the MF analysis characteristics of the damaged parts.
2) Pure tungsten and HPM1800, which contained 5% of dopants, behaved somewhat predictably, yet differently from each other according to the MF charts (although W original surface SEM images were noticeably brighter than HPM1800, and they were dominated by different types of surface defects).
3) Based on the SEM images of the given surface defects, not so clear correlations existed between the MF graphs of the alloy HPM1850, which contained 3% of dopants.

ACKNOWLEDGEMENTS

This work was supported by the International Atomic Energy Agency Coordinated Research Project F13016 (grant No. RC-24179), by the European Union through the Regional Development Fund (TK141), Estonian Research Council grant (PRG1023), and the European Union through the European Regional Development Fund Project (2014-2022.4.01.16-0033 TLÜ TEE). The publication costs of this article were covered by the Estonian Academy of Sciences.

REFERENCES

1. Loarte, A., Saibene, G., Sartori, R., Riccardo, V., Andrew, P., Paley, J. et al. Transient heat loads in current fusion experiments, extrapolation to ITER and consequences for its operation. *Phys. Scr.,* 2007, **T128**, 222–228.
2. Pitts, R. A., Bonnin, X., Escourbiac, F., Frerichs, H., Gunn, J. P., Hirai, T. et al. Physics basis for the first ITER tungsten divertor. *Nucl. Mater. Energy,* 2019, **20,** 100696. https://doi.org/10.1016/j.nme.2019.100696
3. Hirai, T., Barabash, V., Escourbiac, F., Durocher, A., Ferrand, L., Komarov, V. and Merola, M. ITER divertor materials and manufacturing challenges. *Fusion Eng. Des*., 2017, **125**, 250–255. https://doi.org/10.1016/j.fusengdes.2017.07.009
4. Huber, A., Arakcheev, A., Sergienko, G., Steudel, I., Wirtz, M., Burdakov, A. V. et al. Investigation of the impact of transient heat loads applied by laser irradiation on ITER-grade tungsten. *Phys. Scr*., 2014, **T159**, 014005.
5. Paju, J., Väli, B., Laas, T., Shirokova, V., Laas, K., Paduch, M. et al. Generation and development of damages in double forged tungsten in different combined regimes of irradiation with extreme heat loads. *J. Nucl. Mater.*, 2017, **495**, 91–102. https://doi.org/10.1016/j.jnucmat.2017.07.042
6. Herashchenko, S. S., Girka, O. I., Surovitskiy, S. V., Makhlai, V. A., Malykhin, S. V., Myroshnyk, M. O. et al. Effect of sequential steady-state and pulsed hydrogen plasma loads on structure of textured tungsten samples. *Nucl. Instrum. Methods Phys. Res. Sect. B: Beam Interact. Mater. At.*, 2019, **440,** 82–87. https://doi.org/10.1016/j.nimb.2018.12.010
7. Umstadter, K. R., Rudakov, D. L., Wampler, W., Watkins, J. G. and Wong, C. P. C. Effect of ELMs on deuterium-loaded-tungsten plasma facing components. *J. Nucl. Phys. Mater.*, 2011, **415** (Suppl.), S83–S86. https://doi.org/10.1016/j.jnucmat.2010.11.104
8. Yajima, M., Ohno, N., Kajita, S., De Temmerman, G., Bystrov, K., Bardin, S. et al. Investigation of arcing on fiber-formed nanostructured tungsten by pulsed plasma during steady state plasma irradiation. *Fusion Eng. Des.,* 2016, **112**, 156–161. https://doi.org/10.1016/j.fusengdes.2016.07.026
9. Lemahieu, N., Linke, J., Pintsuk, G., Van Oost, G., Wirtz, M. and Zhou, Z. Performance of yttrium doped tungsten under 'edge localized mode'-like loading conditions. *Phys. Scr.,* 2014, **T159**, 014035.
10. Tan, X., Luo, L., Chen, H., Zhu, X., Zan, X., Luo, G. et al. Mechanical properties and microstructural change of W–Y_2O_3 alloy under helium irradiation. *Sci. Rep.,* 2015, **5**, 12755.
11. Shirokova, V., Laas, T., Ainsaar, A., Priimets, J., Ugaste, Ü., Väli, B. et al. Armor materials' behavior under repetitive dense plasma shots. *Phys. Scr.,* 2014, **T161**, 014045.
12. Shirokova, V., Laas, T., Ainsaar, A., Priimets, J., Ugaste, Ü., Demina, E. V. et al. Comparison of damages in tungsten and tungsten doped with lanthanum-oxide exposed to dense deuterium plasma shots. *J. Nucl. Phys.*, 2013, **435**, 181–188. https://doi.org/10.1016/j.jnucmat.2012.12.027
13. Zhang, X. and Yan, Q. Morphology evolution of La_2O_3 and characteristic in W-La_2O_3 alloy under transient heat loading. *J. Nucl. Phys.*, 2014, **451**, 283–291. https://doi.org/10.1016/j.jnucmat.2014.04.001
14. Vilémová, M., Pala, Z., Jäger, A., Matějíček, J., Chernyshova, M., Kowalska-Strzęciwilk, E. et al. Evaluation of surface, microstructure and phase modifications on various tungsten grades induced by pulsed plasma loading. *Phys. Scr.*, 2016, **91**, 034003.
15. Makhlai, V. A., Garkusha, I. E., Linke, J., Malykhin, S. V., Aksenov, N. N., Byrka, O. V. et al. Damaging of tungsten and tungsten-tantalum alloy exposed in ITER ELM-like conditions. *Nucl. Mater. Energy*, 2016, **9**, 116–122. https://doi.org/10.1016/j.nme.2016.04.001
16. Luo, L., Shi, J., Lin, J., Zan, X., Zhu, X., Xu, Q. and Wu, Y. Microstructure and performance of rare earth element-strengthened plasma-facing tungsten material. *Sci. Rep.*, 2016, **6**, 32701.
17. Nogami, S., Guan, W. H., Hattori, T., James, K. and Hasegawa, A. Improved structural strength and lifetime of monoblock divertor targets by using doped tungsten alloys under cyclic high heat flux loading. *Phys. Scr.*, 2017, **T170**, 014011.
18. Nogami, S., Pintsuk, G., Matsui, K., Watanabe, S., Wirtz, M., Loewenhoff, T. and Hasegawa, A. Thermal shock behavior of potassium doped and rhenium added tungsten alloys. *Phys. Scr.*, 2020, **T171**, 014020.
19. Martsepp, M., Laas, T., Laas, K., Priimets, J., Tõkke, S. and Mikli, V. Dependence of multifractal analysis parameters on the darkness of a processed image. *Chaos, Solitons and Fractals*, 2022, **156**, 111811. https://doi.org/10.1016/j.chaos.2022.111811
20. Tõkke, S., Laas, T., Priimets, J., Mikli, V. and Antonov, M. Impact of pulsed deuterium plasma irradiation on dual-phase tungsten alloys. *Fus. Engin. Des.*, 2021, **164**, 112215. https://doi.org/10.1016/j.fusengdes.2020.112215
21. Soesoo, A., Kalda, J., Bons, P., Urtson, K. and Kalm, V. Fractality in geology: a possible use of fractals in the studies of partial melting processes. *Proc. Estonian Acad. Sci. Geology*, 2004, **53**(1), 13–27. https://doi.org/10.3176/geol.2004.1.02
22. Makowiec, D., Rynkiewicz, A., Gałaska, R., Wdowczyk-Szulc, J. and Żarczyńska-Buchowiecka, M. Reading multifractal spectra: Aging by multifractal analysis of heart rate. *Europhys. Lett.,* 2011, **94**(6), 68005. https://doi.org/10.1209/ 0295-5075/94/68005
23. Frankhauser, P., Tannier, C., Vuidel, G. and Houot, H. An integrated multifractal modelling to urban and regional

planning. *Comput. Environ. Urban Syst*., 2018, **67**, 132–146. https://doi.org/10.1016/j.compenvurbsys.2017.09.011
24. Rendón de la Torre, S., Kalda, J., Kitt, R. and Engelbrecht, J. Fractal and multifractal analysis of complex networks: Estonian network of payments. *Europ. Phys. J. B.*, 2017, **90**(12), 1–13. https://doi.org/10.1140/epjb/e2017-80214-5
25. Jafari, A., Tahani, K., Dastan, D., Asgary, S., Shi, Z., Yin, X. T. et al. Ion implantation of copper oxide thin films; statistical and experimental results. *Surf. Interfaces*, 2020, **18**, 100463. https://doi.org/10.1016/j.surfin.2020.100463
26. Ţălu, Ş., Contreras-Bulnes, R., Morozov, I. A., Rodríguez-Vilchis, L. E. and Montoya-Ayala, G. Surface nanomorphology of human dental enamel irradiated with an Er:YAG laser. *Laser Phys.*, 2016, **26**, 025601. https://doi.org/10.1088/1054-660X/26/2/025601
27. Kajita, S., Yoshida, N., Ohno, N. and Tsuji, Y. Growth of multifractal tungsten nanostructure by He bubble induced directional swelling. *New J. Phys*., 2015, **17**, 043038. https://doi.org/10.1088/1367-2630/17/4/043038
28. Das, A., Yadav, R. P., Chawla, V., Kumar, S., Ţălu, Ş., Pinto, E. P. and Matos, R. S. Analyzing the surface dynamics of titanium thin films using fractal and multifractal geometry. *Mater. Today Commun*., 2021, **27**, 102385. https://doi.org/10.1016/j.mtcomm.2021.102385
29. Budaev, V. P., Takamura, S., Ohno, N. and Masuzaki S. Superdiffusion and multifractal statistics of edge plasma turbulence in fusion devices. *Nucl. Fusion*, 2006, **46**, S181. https://doi.org/10.1088/0029-5515/46/4/S10
30. Ţălu, Ş., Matos, R. S., Pinto, E. P., Rezaee, S. and Mardani, M. Stereometric and fractal analysis of sputtered Ag-Cu thin films. *Surf. Interfaces*, 2020, **21**, 100650. https://doi.org/10.1016/j.surfin.2020.100650
31. Shakoury, R., Rezaee, S., Mwema, F., Luna, C., Ghosh, K., Jurečka, S. et al. Multifractal and optical bandgap characterization of Ta_2O_5 thin films deposited by electron gun method. *Opt. Quantum Electron.,* 2020, **52**, 95. https://doi.org/10.1007/s11082-019-2173-5
32. Shakoury, R., Arman, A., Ţălu, Ş., Ghosh, K., Rezaee, S., Luna, C. et al. Optical properties, microstructure, and multifractal analyses of ZnS thin films obtained by RF magnetron sputtering. *J. Mater. Sci. Mater. Electron*., 2020, **31**(7), 5262–5273. https://doi.org/10.1007/s10854-020-03086-3
33. Jelinek, H. F., Milošević, N. T., Karperien, A. and Krstonošić, B. Box-counting and multifractal analysis in neuronal and glial classification. In *Advances in Intelligent Systems and Computing* (Dumitrache, I., ed.). Springer, Berlin, Heidelberg, 2013, 177–189. https://doi.org/10.1007/978-3-642-32548-9_13
34. Fu, H., Wang, W., Chen, X., Pia, G. and Li, J. Fractal and multifractal analysis of fracture surfaces caused by hydrogen embrittlement in high-Mn twinning/transformation-induced plasticity steels. *Appl. Surf. Sci*., 2019, **470**, 870–881. https://doi.org/10.1016/j.apsusc.2018.11.179
35. Tang, W. and Wang, Y. Fractal characterization of impact fracture surface of steel. *Appl. Surf. Sci*., 2012, **258**(10), 4777–4781. https://doi.org/10.1016/j.apsusc.2012.01.091
36. Martsepp, M., Laas, T., Laas, K., Väli, B., Gribkov, V. A., Paduch, M. and Matulka, R. Multifractal analysis of plasma irradiated tungsten alloy samples. *AIP Conf. Proc*., 2019, **2164**, 100005.
37. Martsepp, M., Laas, T., Laas, K., Priimets, J., Mikli, V. and Antonov, M. Multifractal analysis of high-temperature plasma irradiated tungsten surfaces. *Surf. Topogr.: Metrol. Prop*., 2021, **9**, 035030. https://doi.org/10.1088/2051-672X/ac1dc3
38. Ţălu, Ş., Guzzo, P. L., Astinchap, B. and Ghanbaripour, H. Multifractal analysis of ultrasonically machined surfaces of cylindrical quartz crystals: the effect of the abrasive grits. *Surf. Topogr.: Metrol. Prop*., 2021, **9**, 045051. https://doi.org/10.1088/2051-672x/ac459c

Pinnadefektide ja kahjustamata piirkondade multifraktaalsete parameetrite võrdlus

Merike Martsepp, Tõnu Laas, Siim Tõkke, Jaanis Priimets ja Valdek Mikli

Uuringus käsitletakse kolme erinevat materjali (puhas volfram ja kaks volframisulamit Fe ja Ni lisanditega), mida on kiiritatud 20 või 25 ja 100 kõrgtemperatuurse deuteeriumiplasma pulsiga. Seejärel on analüüsitud kahjustatud piirkondade jaotust kiiritatud pindadel ning kahjustamata piirkondade jaotumise omadusi, kasutades selleks multifraktaalanalüüsi. Leiti, et mittekahjustatud pindade jaotuse multifraktaalanalüüsi parameetrite keskväärtused hajuvad vähem kui kahjustuste jaotuse analüüsi tulemused. Selgus kehtiv tendents, et mida heledam on algne sisendpilt, seda täpsemad on tulemused mittekahjustatud pinna uurimisel multifraktaalsete karakteristikute abil.